

Research Article

Analysis of Extent of Deformation Range and Failure Characteristics of Rocks Surrounding a Tunnel Crossing Fault Zone Based on FDEM

Guo Xiaoxiong,^{1,2} Wang Ning ,³ Xu Xueliang,^{1,2} and Ye Zihui³

¹Railway Engineering Research Institute, China Academy of Railway Sciences Corporation Limited, Beijing 100081, China

²State Key Laboratory for Track Technology of High-Speed Railway, Beijing 100081, China

³Jiangxi Key Laboratory of Infrastructure Safety Control in Geotechnical Engineering, East China Jiaotong University, Nanchang 330013, China

Correspondence should be addressed to Wang Ning; wn1290@163.com

Received 23 May 2022; Accepted 24 June 2022; Published 10 August 2022

Academic Editor: Pengjiao Jia

Copyright © 2022 Guo Xiaoxiong et al. This is an open access article distributed under the Creative Commons Attribution License, which permits unrestricted use, distribution, and reproduction in any medium, provided the original work is properly cited.

The combined finite-discrete element method (FDEM) and laboratory test were selected to study the extent of deformation range and time-dependent deformation of surrounding rock during tunnel excavation without support in a fault-crossing tunnel project. FDEM was found to accurately reflect the deformation and failure characteristics of different surrounding rocks during stress release, including conjugate shear and extrusion. Analysis of the results showed that the disturbance range of surrounding rocks could reach 1.5 to 2.5 times the tunnel diameter when crossing the fault zone. The rock surrounding the tunnel was found to incur significant conjugate shear deformation and extrusion deformation: conjugate shear deformation was identified as dominant in the deep rock mass, whereas extrusion deformation prevailed in the rock mass near the cave wall. The conjugate shear distribution was represented as a spiral line of deformation circling around the tunnel section, with an elliptical main deformation zone with its long axis parallel to the fault plane. Compared with the findings when crossing the intact rock mass, the deformation of the surrounding rocks when crossing the fault zone was characterized by rapid development, deep expansion area, and large deformation. The study conclusions were that supporting bolts and steel arches should be implemented timely when excavating fault zones and that both lithology and optimal construction timing were essential considerations in determining the length of the supporting bolts.

1. Introduction

Due to the diversity of stratigraphic conditions, it may be necessary for many mountain tunnels to cross fault zones, some of which may be active. Active fault zones are often accompanied by varying degrees of unfavorable geological conditions. For example, rock mass characteristics within fault zones usually include high susceptibility to fracturing and weathering, poor strength, and significant differences from the surrounding rock. When a tunnel passes through a fault zone, considerable deformation occurs, potentially alongside serious problems such as tunnel face instability, collapsing of the tunnel wall, and supporting structural

failure [1–5]. In his study, Terzaghi [6] ascribed the large extrusion deformation in the tunnel to the considerable amount of clay minerals present in the rock, suggesting that the volume of this rock mass slowly increased and then intruded into the tunnel clearance. The actual sampling at the engineering site showed that the rock mass within a certain range of the fault zone and its surrounding area contained very high clay minerals. Terzaghi [6] therefore concluded that the deformation in the vicinity of the tunnel crossing fault zone could be attributed to the significant deformation of local soft rocks.

Extensive research has been carried out on fault-crossing tunnels, including analysis models, experiments, and numerical

simulation. Key influencing factors of fault zones studied have included the fault zone width, soil properties, and the intersection angle between tunnel axis and fault zone [7, 8]. Tunnelling research subjects have encompassed surrounding rock deformation, internal forces, tunnel lining deformation, and the advantages and drawbacks of a range of construction measures [9–13]. In many research hot-spots, the deformation of surrounding rocks during excavation has been ignored, that is, the development of crack or deformation of rock mass around the tunnel in the vertical direction, especially in the engineering project crossing the active fault zone. Since active fault zones are usually accompanied by high tectonic stresses, tunnel excavations produce a release of initial stress in the rock mass. This stress release leads to a deep deformation of surrounding rocks, the most significant instance being the rock burst phenomenon of hard rock with high ground stress. A stress release gradient change occurs from the inner wall of the tunnel to the rock mass, causing problematic issues such as the area of influence of rock mass deformation, and the potential presence of cracks in the rock mass. Fractures within the rock mass have important repercussions on the waterproofing and drainage maintenance systems throughout the tunnel operation period. Rigorous research is therefore urgently required on this subject.

To date, numerical simulation has been the most favored method for tunnel analysis, commonly using numerical software such as FLAC3D, Plaxis, and ABAQUS [14–17]. The finite-discrete element method is a common numerical tool to analyze fracture development, in particular the typical one is the combined finite-discrete element method (FDEM) [18–23]. It can simulate the behavioral process of materials from continuous deformation to discontinuous deformation. In the field of civil engineering, this method has been applied to analyze the deformation of rocks surrounding highway construction and the development of cracks in concrete structures and to perform simulation tests of the mass strength of various rock and soil types [24–27], all of which demonstrated good computational and simulation performances.

In the present study, set in an engineering context of a tunnel crossing a fault zone, laboratory testing and the FDEM were implemented to establish the law determining the area affected by rock mass deformation caused by tunnel excavation around the site where the tunnel crossed the fault zone. The failure mechanism of rock mass within the fault zone was revealed, which in the authors' view provided valuable references for preventive measures against rock deformation in future projects involving tunnel excavations.

2. Basic Principles of FDEM Numerical Simulation

FDEM was first proposed by Munjiza et al. [28–30] in 1995. In 2004, they proposed a complete set of theories and developed the corresponding calculation program Y-Code. However, as the initial version of the computation program, the Y-Code still presents numerous problems to this day. For example, quasistatic friction is not achieved, contact energy

dissipation is not considered, and the Mohr–Coulomb shear strength criterion is not realized. Therefore, Mahabadi et al. proposed an improved version of Y-Geo in 2012 based on the Y-Code [31], which made the FDEM constitutive model and strength criterion more consistent with the mechanical properties of rock materials. Moreover, a corresponding preprocessor Y-GUI [32] was developed to quickly assign corresponding attributes to model elements and nodes.

The basic principle of FDEM can be summarized as follows: the intact material was divided into triangular elements, and quadrilateral joint elements with initial zero thickness were inserted at the boundary of the triangular elements. The longest side of the quadrilateral elements was shared with a triangular element, and the shortest side of the quadrilateral elements coincided with the line of adjacent nodes, as shown in Figure 1(a) (the initial thickness exists). The triangular elements represented the constant strain elements, and their Cauchy deformation stress was solved by the generalized application of Hooke's law. Moreover, the triangular elements only sustained elastic deformation, as opposed to plastic deformation or fracture failures. The plastic yield and fracture failure of rock materials were represented by the quadrilateral joint elements. The state of the quadrilateral joint elements was determined according to the relative tensile or shear displacement between nodes, as shown in Figure 1(b). When two of the three nodes in the quadrilateral elements (points A, B, and C in Figure 1(a)) reached either the ultimate tensile displacement or the shear displacement s_r , the fracture failure occurred in the joint elements. The triangular elements were transformed on both sides from a bonding relationship to a contact relationship. The bond stress calculation program for the joint elements was no longer implemented and the contact stress was solved by potential functions. The advantage of potential functions was that the contact stress consisted of distributed stress rather than concentrated stress, which was more consistent with the real contact relationship of the block, thus avoiding the need to conduct fillet processing.

The constitutive equations of the quadrilateral joint element were

$$\sigma_n = \begin{cases} \frac{o}{o_p} \cdot f_t, o < o_p, \\ z \cdot f_t, o_p < o < o_t, \end{cases}$$

$$\tau = \begin{cases} \frac{s}{s_p} \cdot c, s < s_p \text{ and } \sigma_n > 0, \\ \frac{s}{s_p} \cdot (c - \sigma_n \tan \varphi_i), s < s_p \text{ and } \sigma_n < 0, \\ z \cdot c, s_p < s < s_t \text{ and } \sigma_n > 0, \\ z \cdot c - \sigma_n \tan \varphi_i, s_p < s < s_t \text{ and } \sigma_n < 0, \end{cases} \quad (1)$$

where σ_n and τ are normal and tangential stresses ($\sigma_n > 0$ represents tensile stress, and $\sigma_n < 0$ represents compressive stress); o and s are normal and tangential displacements; o_p

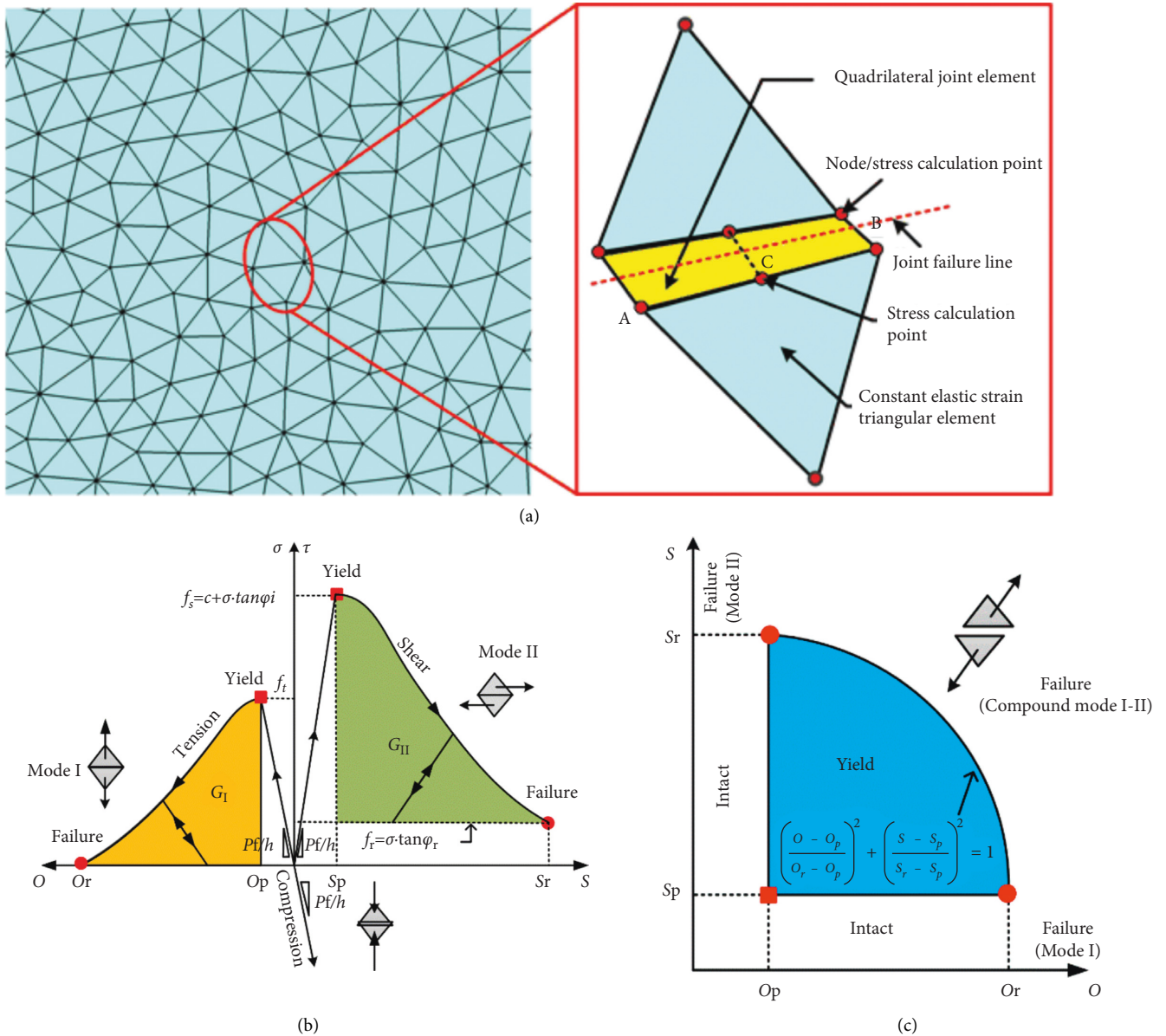


FIGURE 1: Triangular meshing and failure modes of joint elements.(a) Triangular and quadrilateral grids. (b) Failure modes I and II. (c) Compound failure modes I and II.

and s_p are normal and tangential peak displacements; and o_t and s_t are normal and tangential ultimate displacements. It can be observed that when the tensile or shear displacement of the joint element reached its corresponding limit value, the joint element fractured and failed; c is the cohesion; ϕ_i is the internal friction angle; f_t is the tensile strength; and z is the post-peak softening function [33].

3. Project Overview

The rock strata around the tunnel line mainly consisted of quartz sandstone, slate, and quartz diorite. The tunnel crossed an active fault zone with a small angle. The fault zone was a normal fault with a dip angle of $64\sim 80^\circ$. The width of the core fault zone was about 7 m, and the width of the fault

zone was about 60 m. The tunnel was about 235 m deep, while the depth of groundwater was about 5 m. The results of the ground stress tests showed that the horizontal ground stress of surrounding rocks was dominant, which was measured at about 17.5 MPa. At the same time, the rock mass near the fault zone was fractured and formed part of an area of significant, widespread deformation, which was prone to major tunnel deformation. The tunnel was a double-line tunnel with a diameter (d) of about 13.5 m and an included angle between the tunnel axis and fault strike of about 14° . The plane relationship between tunnel and fault is shown in Figure 2. According to the tunnel crossing the strata, three working cases were selected: (I) the tunnel crossed the intact rock mass; (II) the tunnel crossed the fault fracture zone; and (III) the tunnel crossed the fault core

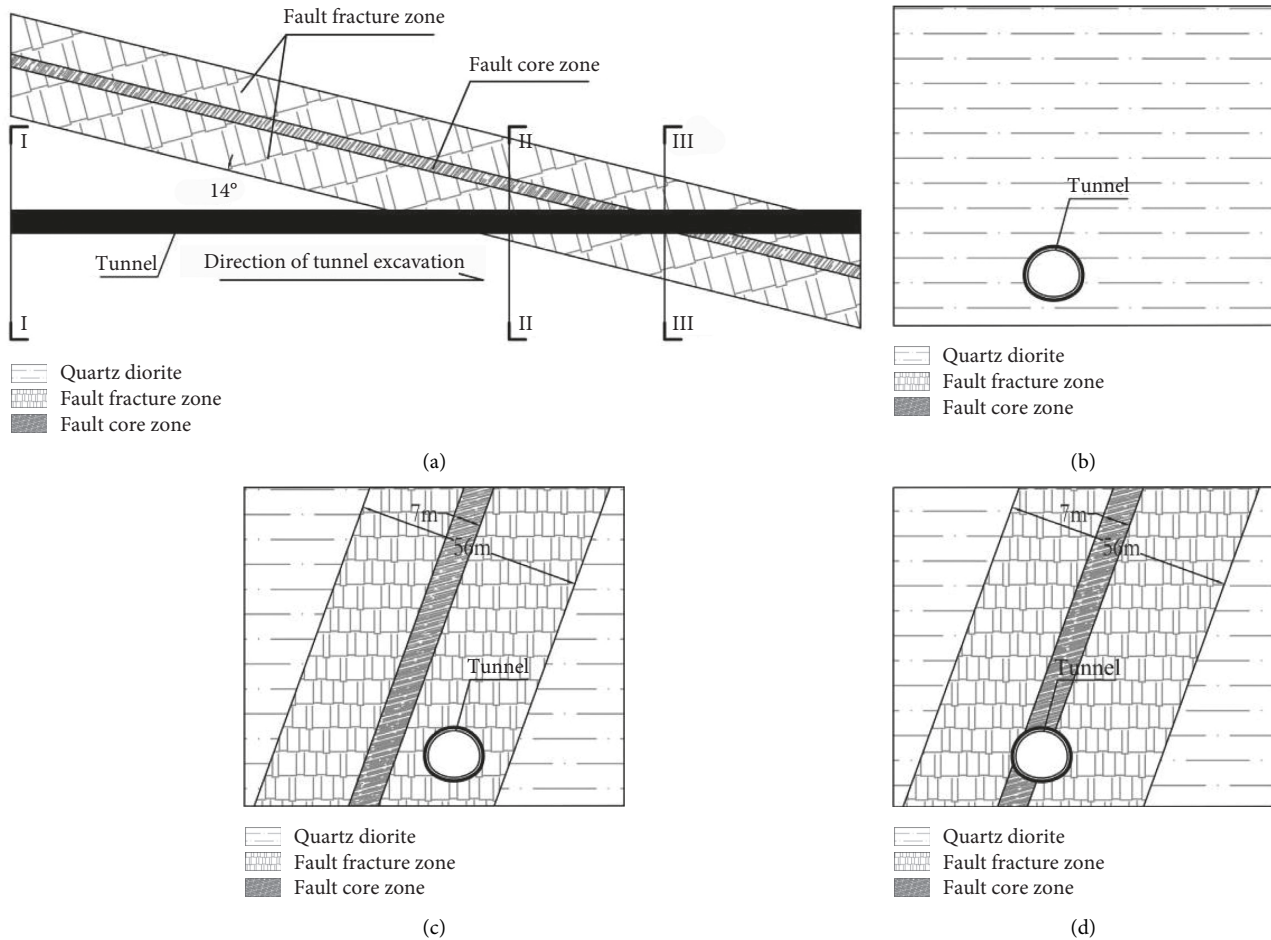


FIGURE 2: Plane schematic diagram of tunnel crossing fault zone. (a) Cross-section. (b) I-I profile section. (c) II-II profile section. (d) III-III profile section.

zone. Then, the difference in deformation of the surrounding rocks was compared and analyzed at the point where the tunnel effectively crossed the fault zone.

4. Soil Parameter Test

Rock samples representing different rock masses in three typical sections were obtained from different excavation locations along the tunnel. The three types of rock samples were as follows: (a) weakly weathered quartz diorite representing the original rock; (b) highly weathered quartz sandstone representing the fault zone; and (c) fully weathered soil representing the fault core zone.

The production process and core samples of quartz diorite are shown in Figure 3. The core size was 50 mm in diameter and 100 mm in height. The mineral composition and mechanical properties of the rock samples were tested. The main minerals in the rock samples were potassium feldspar, albite, and quartz. Saturated uniaxial compressive strength tests and Brazilian splitting tests were conducted on the samples, and the test results are shown in Table 1.

The rock samples of strongly weathered quartz sandstone are shown in Figure 4. In their natural state, the rock samples were massive and without any obvious structural cleavage. It thus proved challenging to obtain regular cores

using the sampler, and the rock samples could be crushed by hand. The saturated uniaxial compressive strength of the rock samples was less than 1 MPa. The initial average water content and initial density of the rock samples were 1.8% and 2.49 g/cm³, respectively. The rock samples were mainly composed of albite and quartz with poor resistance to disintegration. Due to the weakness of the rock samples, they were destroyed and remodeled; the triaxial consolidated drained tests were carried out. The soil parameters obtained in the test are shown in Table 2.

The rock mass in the fault core zone had essentially been fully weathered into the soil, as shown in Figure 5. The soil samples were found to belong to gravel soil, and the grains mainly consisted of sand while also containing some clay and block stones. The block stone size distribution was mainly between 20 and 150 mm. A triaxial consolidated drained test was performed on the undisturbed soil samples containing block stones. The soil parameters obtained in the test are shown in Table 2.

5. Numerical Model

The FDEM numerical simulation model was established on the basis of three different profiles, as shown in Figure 6. The model size was 140 m × 140 m and was divided into three



FIGURE 3: Production process and core samples of quartz diorite. (a) Core processing. (b) Rock samples. (c) Rock triaxial loading device.

TABLE 1: Strength parameters of rock samples.

Experiment content	Test strength (MPa)	Mean value (MPa)
Saturated uniaxial compressive strength	93.00	102.44
	97.86	
	116.45	
Saturated Brazilian splitting test	2.55	2.18
	2.26	
	1.73	



FIGURE 4: Strongly weathered quartz sandstone and test instruments. (a) Strongly weathered quartz sandstone. (b) GDS hollow cylinder torsional shear instrument.

TABLE 2: Test soil parameters.

Soil name	Density (g/cm^3)	Cohesion (kPa)	Internal friction angle ($^\circ$)
Strongly weathered quartz sandstone	2.49	14.5	35.4
Fully weathered soil in the fault core zone	2.26	3.7	35.8

sectors: a tunnel sector, a mesh refinement sector, and a far-field sector. The diameters of the tunnel and the mesh refinement areas were 13.5 m and 60 m, respectively. The mesh sizes of the tunnel boundary and the model boundary were 0.15 m and 10 m, respectively. Under two-dimensional plane strain conditions, the tunnel excavation process could be divided into two stages: a ground stress loading stage and a tunnel excavation stage. The model boundary was free at the ground stress stage and fixed at the tunnel excavation stage. After the ground stress had been

applied and the model reached equilibrium, a core material softening method was adopted to reflect the gradual weakening process of the radial support effect on the tunnel face. In other words, the elastic modulus and viscous damping of the material in the tunnel region were gradually weakened, and the softening of each step had to ensure that the response of surrounding rocks caused by the softening of the previous step reached equilibrium before it could be performed. The input parameters are the ones listed in Table 3.

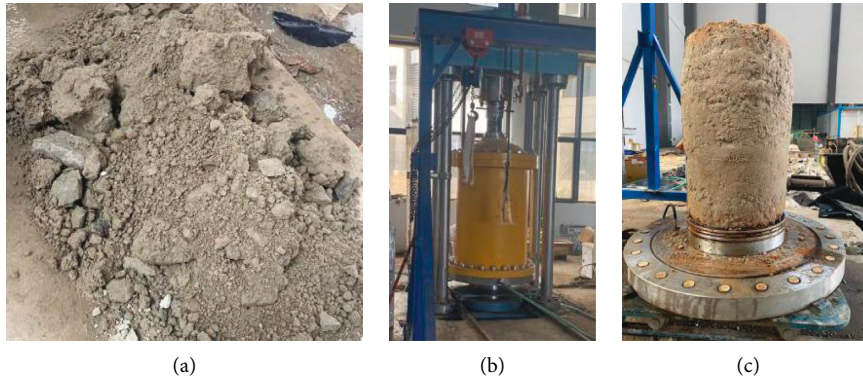


FIGURE 5: Soil samples in the fault core zone and testing instruments. (a) Soil sample in the fault core zone. (b) Triaxial tester. (c) Soil sample after the test.

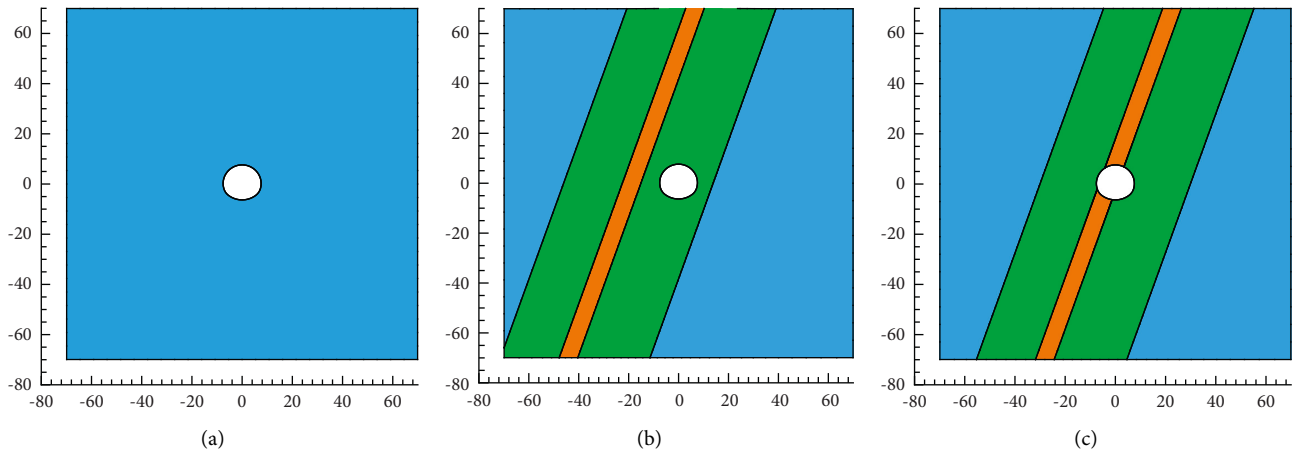


FIGURE 6: The FDEM numerical model. (a) Crossing the intact rock (case 1). (b) Crossing the fault fracture zone (case 2). (c) Crossing the fault core zone (case 3).

TABLE 3: Input parameters of tunnel excavation introduced in the FDEM numerical model.

Parameter	Mildly weathered quartz diorite	Strongly weathered quartz sandstone	Fully weathered soil
Triangular element parameter			
Density, ρ (kg/m ³)	2490	2490	2260
Elastic modulus, E (GPa)	50	25	20
Poisson's ratio, ν	0.25	0.25	0.25
Mesh size around the tunnel, h (m)	0.15	0.15	0.15
Viscous damping, μ (kg/m·s)		$2h\sqrt{E\rho}$	
Calculation step, Δt (s)		$1e-7$	
Quadrilateral joint element parameter			
Tensile strength, f_t (kPa)	2180	4.2	1.3
Cohesion, c (kPa)	7000	14.5	3.7
Type I fracture energy, G_I (J/m ²)	10,000	1,000	400
Type II fracture energy, G_{II} (J/m ²)	20,000	4,000	1,000
Internal friction angle, φ_i (°)	28	35.4	35.8
Sliding friction angle, φ_r (°)	28	35.4	35.8
Normal contact stiffness, P_n (GPa)	100	50	40
Tangential contact stiffness, P_t (GPa)	100	50	40
Joint penalty, P_f (GPa)	100	50	40

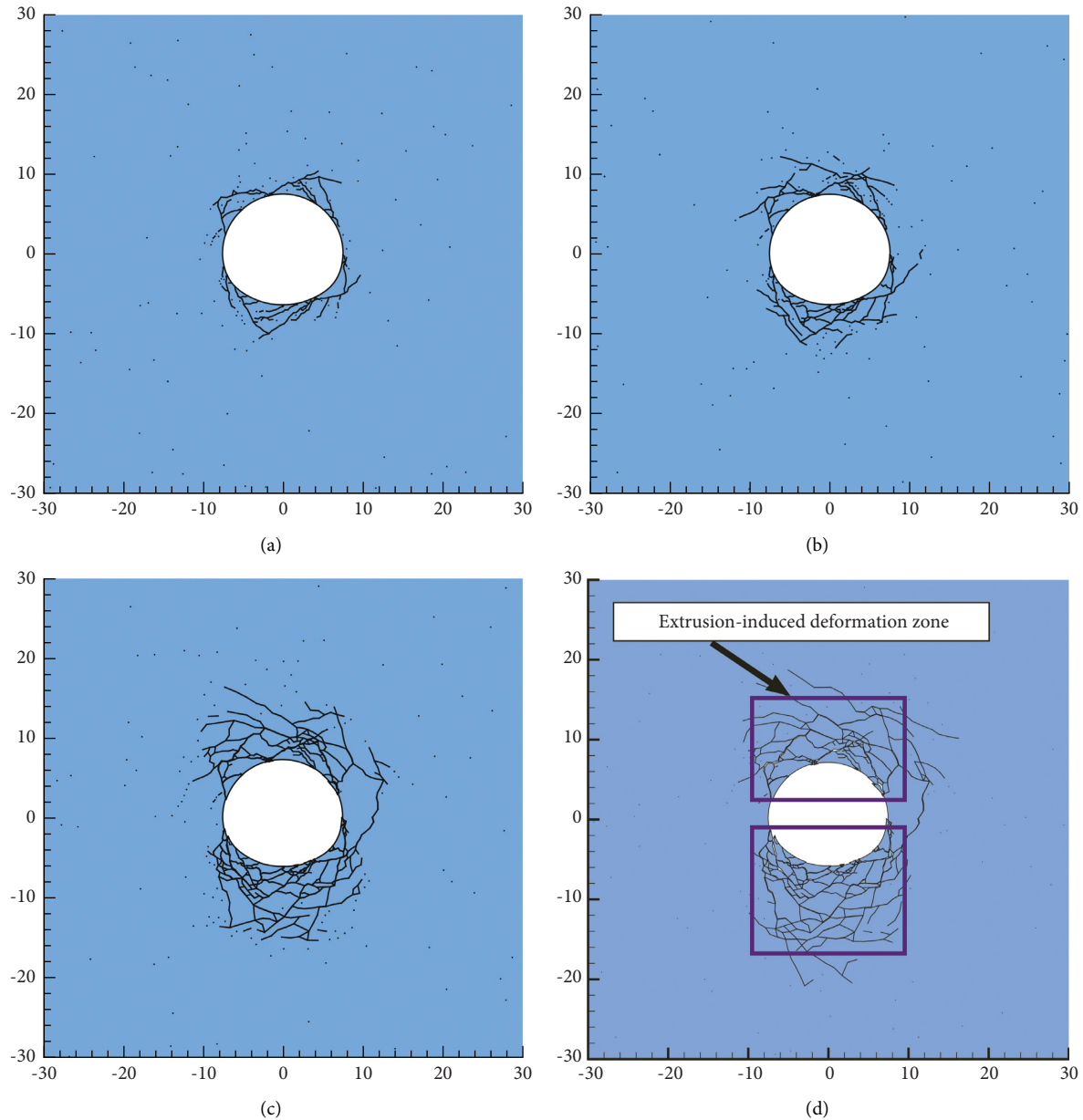


FIGURE 7: Development of the law determining the area of surrounding rock deformation (case 1). (a) 2.1 million step. (b) 2.4 million step. (c) 3.0 million step. (d) 4.2 million step.

6. Data Calculation and Analysis

6.1. Development of an Analysis Method of the Area of Surrounding Rock Deformation during Excavation of the Intact Rock Mass. Figure 7 shows the regional development of deep deformation of surrounding rocks caused by stress release during tunnel excavation of the intact rock mass without support. At the initial stage of excavation, the deformation development area was found to be shallow, mainly occurring at the top and bottom of the tunnel. With the further distribution of stress release of the surrounding rock to the deep area, the deformation zone expanded further and eventually reached an area equal to one time the hole diameter. Within 0.1 d of the vault, the obvious surrounding rock fracture occurs.

6.2. Analysis Development of the Area of Surrounding Rock Deformation during Excavation of the Fault Fracture Zone. Figure 8 shows the regional development of deep deformation of surrounding rocks caused by stress release during tunnel excavation of the fault fracture zone without support. At the initial stage of excavation, the deformation only occurred within the crushing zone and mainly at the top and bottom of the tunnel, showing distinct conjugate shear deformation characteristics. With the wider distribution of stress release to the deep area of the surrounding rock, the deformation zone expanded further. The side close to the fault core zone was found to have a deeper development area which could exceed 1.5 times the cavity diameter. The conjugate shear line density was significantly

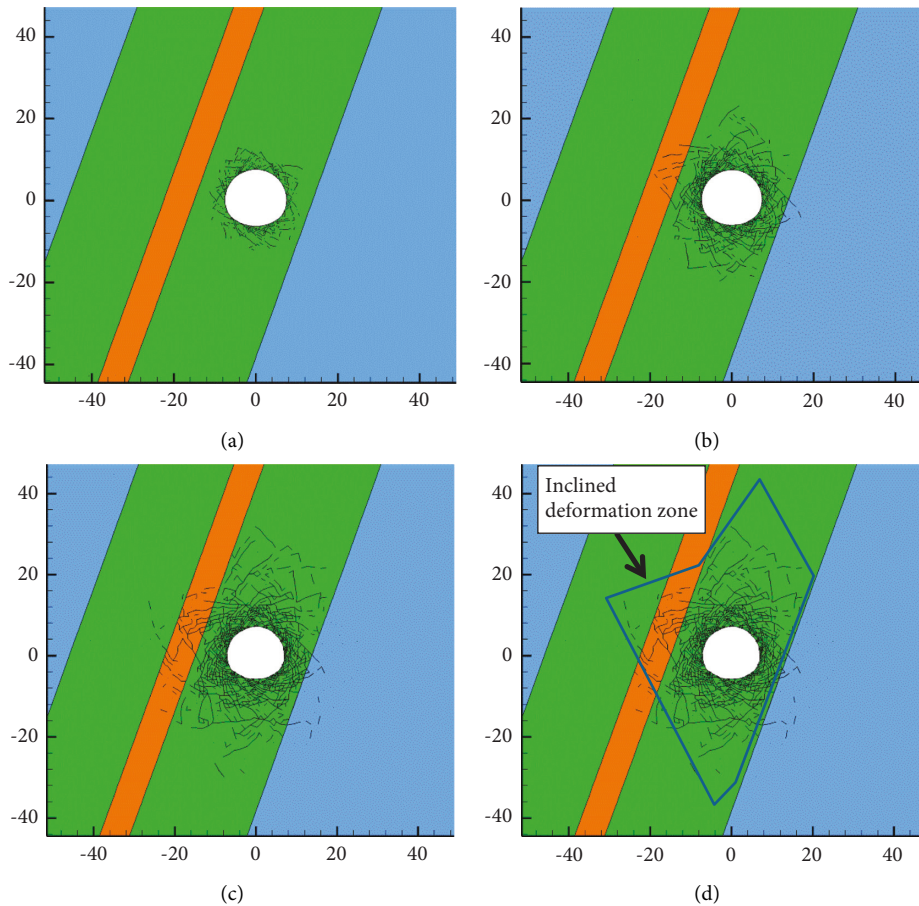


FIGURE 8: Development of the law determining the area of surrounding rock deformation (case 2). (a) 2.1 million step. (b) 2.4 million step. (c) 3.0 million step. (d) 4.2 million step.

higher than that of the intact rock mass excavated. The surrounding rock near the tunnel wall shifted from incurring shear failure to extrusion failure.

6.3. Analysis Development of the Area of Surrounding Rock Deformation during Excavation of the Fault Core Zone. Figure 9 shows the regional development of deep deformation of the surrounding rocks caused by stress release during tunnel excavation of the fault core zone without support. It can be observed that when the fault core zone was being crossed, the surrounding rock deformation zone quickly expanded and that shear deformation and extrusion deformation coexisted at the initial stage of excavation. With the continuous release of stress into the surrounding rock, the deformation zone increased rapidly, whereas the rock mass near the tunnel was mainly characterized by extrusion deformation, the deep rock mass predominantly incurred conjugate shear deformation. The approximate elliptic deformation range was established by taking the axis close to the fault core zone as the long axis, while the main deformation zone could approximately exceed twice the cavity diameter. The conjugate shear line could bypass the tunnel to form a long spiral that snaked its way through up and down, while the main deformation zone formed an ellipse with the long axis parallel to the fault plane.

6.4. Comparative Analysis of Surrounding Rock Deformation Development in Different Excavation Areas. Figure 10(a) shows the final development trend of the surrounding rock deformation zone when crossing the intact rock mass or the fault zone, and the range varied by 2.5 times. Compared with Figures 10(b) and 10(c), the final development depth of the surrounding rock deformation zone was close when crossing the fault fracture zone or the fault core zone, and the deformation was relatively intense. When crossing the fault fracture zone, the dense area of deformation fissures was within the range of 1.0 d. When crossing the fault core zone, the dense area of deformation fissures was within the range of 1.5 d.

The development of the deformation zone can be better observed from the displacement field nephogram of surrounding rocks illustrated in Figure 11. When crossing the intact monolayer rock mass, the main deformation of surrounding rocks was in the range of 7 m (about 0.5 d). The maximum deformation had occurred in the upper and lower sectors adjacent to the tunnel, with a value of about 0.5 m. When crossing the fault fracture zone, the deformation zone of surrounding rocks was within 15 m of the tunnel wall (about 1.0 d). The deformation at the top and bottom of the tunnel was significant, with a maximum of about 0.8 m. When crossing the fault core zone, the deformation area of

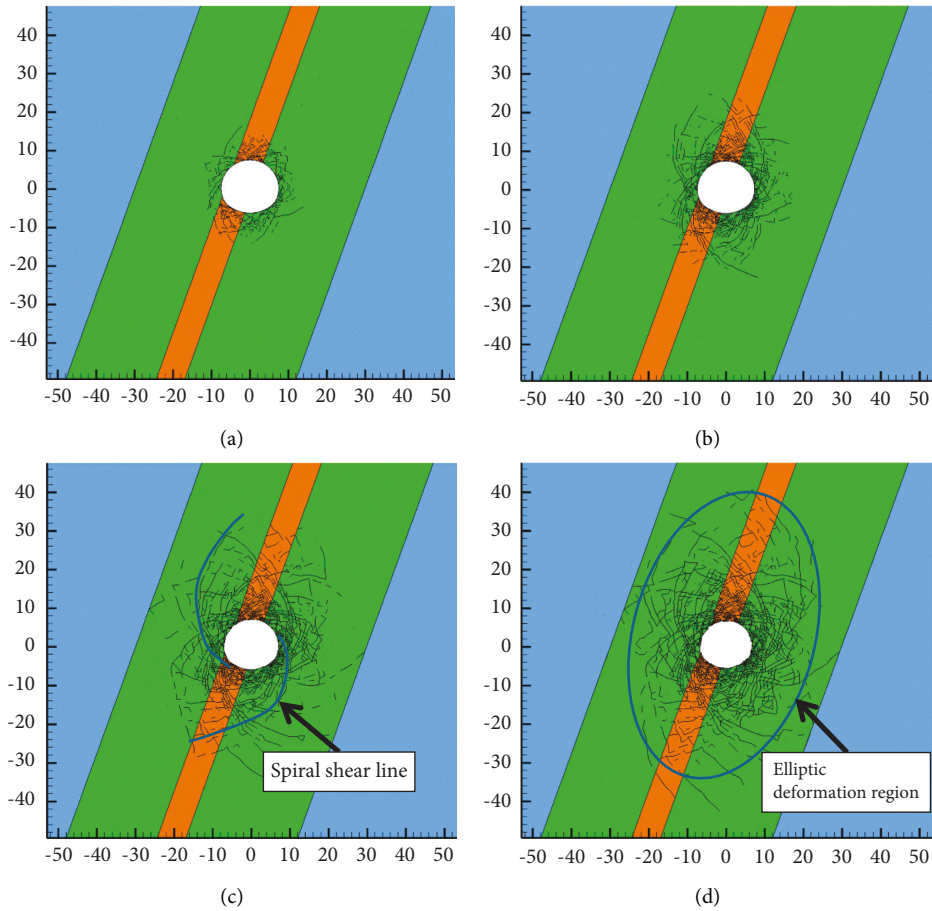


FIGURE 9: Development of the law determining the surrounding rock deformation zone (case 3). (a) 2.1 million step. (b) 2.4 million step. (c) 3.0 million step. (d) 4.2 million step.

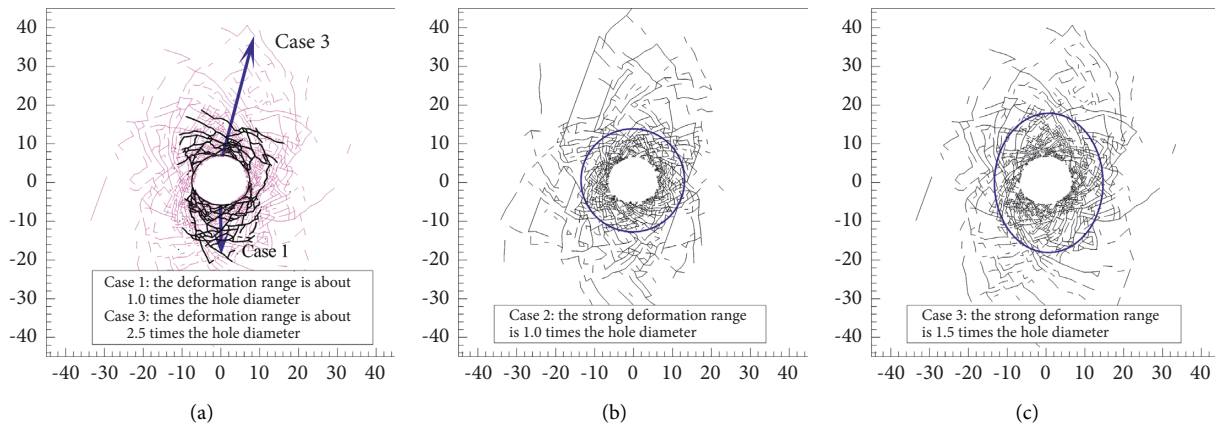


FIGURE 10: Schematic diagram of the development of surrounding rock deformation. (a) Comparison of the deformation range between working cases 1 and 3. (b) Schematic diagram of the strong deformation range in working case 2. (c) Schematic diagram of the strong deformation range in working case 3.

surrounding rocks was within 20 m of the tunnel wall (about 1.5 d). The deformation at the top of the tunnel was significant, with a maximum of about 1.2 m.

Figure 12 shows the maximum development range of surrounding rock deformation zones under different analysis steps (time) after excavation of different rock masses. The slope of the two curves during the excavation of the fault

zone can obviously be observed to be steeper than that during the excavation of the intact rock mass, indicating that the initial deformation developed faster in the fault zone due to the poor properties of the surrounding rocks.

The above analysis is based on unsupported excavation, which is corresponding to the situation in the time interval between the completion of tunnel excavation and the

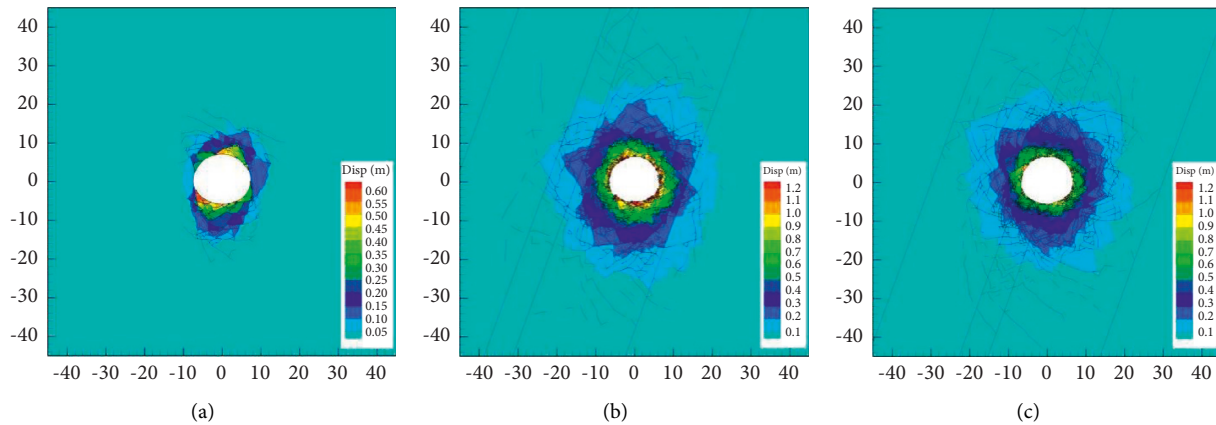


FIGURE 11: Nephogram of surrounding rock deformation and displacement. (a) Crossing the intact rock (case 1). (b) Crossing the fault fracture zone (case 2). (c) Crossing the fault core zone (case 3).

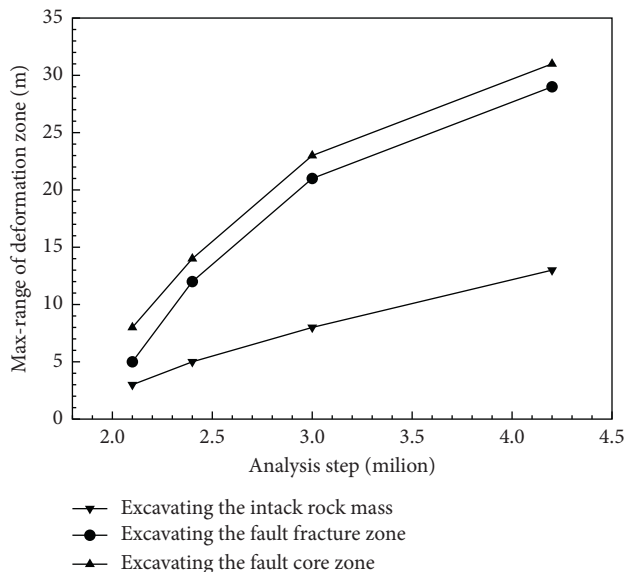


FIGURE 12: Maximum range of the surrounding rock deformation zone at different steps.

implementation of the support system. The increase in the analysis step represents the increase in the time. It can be seen that the deformation range of the surrounding rock is smaller if the supporting system (supporting bolts) is timelier completed. The development rule of the deformation range of the surrounding rock further indicates that the supporting bolt length is correlated with the construction promptness of the support system and the property of the rock mass.

7. Conclusions

In this study based on an actual project, the real rock mass parameters were obtained by analyzing the test results of different surrounding rock samples obtained from the project site. On this basis, the deformation development characteristics of surrounding rocks without support following tunnel excavation were analyzed by using the FDEM. The analysis results showed that

- (1) The rock mass is more disturbed by the stress release from tunnel excavations when these cross a fault zone than under the conditions where tunnel excavations cross an intact rock mass. The range of disturbance can reach 1.5 to 2.5 times the tunnel diameter, and the strong disturbance area (where the displacement exceeds 0.2 m) can reach 1.0 to 1.5 times the tunnel diameter. This will provide guidance for determining the length of the supporting bolts.
- (2) Compared with the extrusion deformation that occurs when a tunnel crosses an intact rock mass, conjugate shear deformation and extrusion deformation coexist when a tunnel crosses a fault zone. Conjugate shear deformation is dominant in the deep rock mass, and extrusion deformation is dominant in the rock mass near the cave wall. Therefore, appropriate supporting measures should be adopted in different zones with different deformation mechanisms.
- (3) When crossing an intact rock mass, the surrounding rock deformations mainly occur in an approximately rectangular range that includes the top and bottom of the cave. No penetrating deformation line bypassed the tunnel section. When a tunnel crosses a fault zone, a spiral deformation line is formed around the tunnel section, and the main deformation zone takes an elliptical shape, the long axis of which lies parallel to the fault plane. This conclusion can provide a reference for the selection of the length of supporting bolts in different directions on the tunnel cross-section.
- (4) Compared with the condition of a tunnel crossing an intact rock mass, the surrounding rock deformation develops more rapidly when a tunnel crosses a fault zone. Depending on the speed and range of development of deformation zones, the difference in length of any supporting bolts affixed to different surrounding rocks is significant. The length of applied bolts is determined both by the properties of

the surrounding rock and the timing of application. In addition, when being implemented in a fault zone, the construction and fitting of supporting bolts and steel arches must be completed timely, thus the fracture deformation of deep surrounding rock can be more efficiently controlled.

Data Availability

Some or all data, models, or code that support the findings of this study are available from the corresponding author upon reasonable request.

Conflicts of Interest

The authors declare that they have no conflicts of interest.

Acknowledgments

The research work was supported by the National Natural Science Foundation of China (Grant nos. 51868021, 52168047, and 41972291), the State Key Laboratory for Track Technology of High-Speed Railway, China Academy of Railway Sciences (Contract no. 2020YJ140), and the Natural Science Foundation of Jiangxi Province (Grant no. S2020QNJB1234).

References

- [1] J. G. Liu, X. J. Zhou, Q. H. Xiao, and W. Zhao, "Fault-related instability problems of tunnels - the host rock slip criterion and characteristics of the tunneling-induced shear displacements," *Stavbni Obzor Civil Engineering Journal*, vol. 26, no. 4, pp. 441–458, 2017.
- [2] G. Bruneau, D. Tyler, J. Hadjigeorgiou, and Y. Potvin, "Influence of faulting on a mine shaft a case study: part I Background and instrumentation," *International Journal of Rock Mechanics and Mining Sciences*, vol. 40, pp. 95–111, 2003.
- [3] L. Meng, T. Li, Y. Jiang, R. Wang, and Y. Li, "Characteristics and mechanisms of large deformation in the Zhegu mountain tunnel on the Sichuan–Tibet highway," *Tunnelling and Underground Space Technology*, vol. 37, pp. 157–164, 2013.
- [4] M. Kun and T. Onargan, "Influence of the fault zone in shallow tunneling: a case study of Izmir Metro Tunnel," *Tunnelling and Underground Space Technology*, vol. 33, pp. 34–45, 2013.
- [5] F. Suorineni, D. Tannant, and P. Kaiser, "Determination of fault-related sloughage in open stopes," *International Journal of Rock Mechanics and Mining Sciences*, vol. 36, no. 7, pp. 891–906, 1999.
- [6] K. Terzaghi, "Rock defects and loads on tunnel supports," in *Rock Tunneling with Steel Supports*, R. V. Proctor and T. L. White, Eds., Commercial Shearing and Stamping Company, Ohio, OH, USA, 1946.
- [7] S. Ma, L. Zhang, D. Wang, X. R. Tan, S. Li, and Y. Liu, "Analysis of tunnel lining failure mechanism under the action of active fault," *Shock and Vibration*, vol. 2021, Article ID 9918021, 11 pages, 2021.
- [8] M. Ghafari, H. Nahazanan, Z. Md Yusoff, and N. N. Nik Daud, "A novel experimental study on the effects of soil and faults' properties on tunnels induced by normal and reverse faults," *Applied Sciences*, vol. 10, no. 11, p. 3969, 2020.
- [9] P. Oreste and D. Pella, "Modelling progressive hardening of shotcrete in convergence-confinement approach to tunnel design," *Tunnelling and Underground Space Technology*, vol. 12, no. 3, pp. 425–431, 1997.
- [10] F. Kimura, N. Okabayashi, and T. Kawamoto, "Tunnelling through squeezing rock in two large fault zones of the Enasan Tunnel II," *Rock Mechanics and Rock Engineering*, vol. 20, no. 3, pp. 151–166, 1987.
- [11] T. Kondo, "The management problem of measurement and control in tunnel construction with the NATM," *Construction Technology*, vol. 11, pp. 76–80, 1977.
- [12] D. Zhang, S. Liu, and S. Reng, "Research on selection of steel and steel grid for tunnel support in soft rock with high geostress," *Chinese Journal of Rock Mechanics and Engineering*, vol. 33, no. 11, pp. 2258–2266, 2014.
- [13] G. Li and Y. Zhu, "Control technology for large deformation of high land stressed weak rock in wushaoling tunnel," *Journal of Railway Engineering Society*, vol. 3, pp. 54–59, 2008.
- [14] Y. Ma, Q. Sheng, G. Zhang, and Z. Cui, "A 3D discrete-continuum coupling approach for investigating the deformation and failure mechanism of tunnels across an active fault: a case study of xianglushan tunnel," *Applied Sciences*, vol. 9, no. 11, p. 2318, 2019.
- [15] H. Lan, C. D. Martin, and B. Hu, "Effect of heterogeneity of brittle rock on micromechanical extensile behavior during compression loading," *Journal of Geophysical Research*, vol. 115, no. B1, 2010.
- [16] W. C. Zhu and C. A. Tang, "Micromechanical model for simulating the fracture process of rock," *Rock Mechanics and Rock Engineering*, vol. 37, no. 1, pp. 25–56, 2004.
- [17] J. F. Hazzard, R. P. Young, and S. C. Maxwell, "Micro-mechanical modeling of cracking and failure in brittle rocks," *Journal of Geophysical Research: Solid Earth*, vol. 105, no. B7, Article ID 16683, 2000.
- [18] T. M. He, Q. Zhao, J. Ha, K. Xia, and G. Grasselli, "Understanding progressive rock failure and associated seismicity using ultrasonic tomography and numerical simulation," *Tunnelling and Underground Space Technology*, vol. 81, pp. 26–34, 2018.
- [19] H. Han, D. Fukuda, H. Liu et al., "Combined finite-discrete element modellings of rockbursts in tunnelling under high in-situ stresses," *Computers and Geotechnics*, vol. 137, Article ID 104261, 2021.
- [20] A. Lisjak, Q. Liu, Q. Zhao, O. K. Mahabadi, and G. Grasselli, "Numerical simulation of acoustic emission in brittle rocks by two-dimensional finite-discrete element analysis," *Geophysical Journal International*, vol. 195, no. 1, pp. 423–443, 2013.
- [21] A. Lisjak, B. S. A. Tatone, O. K. Mahabadi et al., "Hybrid finite-discrete element simulation of the EDZ formation and mechanical sealing process around a microtunnel in opalinus clay," *Rock Mechanics and Rock Engineering*, vol. 49, no. 5, pp. 1849–1873, 2016.
- [22] P. Deng, Q. Liu, X. Huang, Q. Liu, H. Ma, and W. Li, "Acquisition of normal contact stiffness and its influence on rock crack propagation for the combined finite-discrete element method (FDEM)," *Engineering Fracture Mechanics*, vol. 242, no. 6, Article ID 107459, 2021.
- [23] P. Deng and Q. Liu, "Influence of the softening stress path on crack development around underground excavations: insights from 2d-fdem modelling," *Computers and Geotechnics*, vol. 117, Article ID 103239, 2020.
- [24] I. Vazaios, M. S. Diederichs, and N. Vlachopoulos, "Assessment of strain bursting in deep tunnelling by using the finite-

- discrete element method,” *Journal of Rock Mechanics and Geotechnical Engineering*, vol. 11, no. 1, pp. 12–37, 2019.
- [25] W. Wang, Q. Liu, H. Ma, H. Lu, and Z. Wang, “Numerical analysis of material modeling rock reinforcement in 2d fdem and parameter study,” *Computers and Geotechnics*, vol. 126, Article ID 103767, 2020.
- [26] Z. Wu, X. Ji, Q. Liu, and L. Fan, “Study of microstructure effect on the nonlinear mechanical behavior and failure process of rock using an image-based-fdem model,” *Computers and Geotechnics*, vol. 121, Article ID 103480, 2020.
- [27] A. Farsi, A. Bedi, J. P. Latham, and K. Bowers, “Simulation of fracture propagation in fibre-reinforced concrete using fdem: an application to tunnel linings,” *Computational Particle Mechanics*, vol. 7, no. 5, pp. 961–974, 2020.
- [28] A. Munjiza, D. R. J. Owen, and N. Bicanic, “A combined finite-discrete element method in transient dynamics of fracturing solids,” *Engineering Computations*, vol. 12, no. 2, pp. 145–174, 1995.
- [29] A. Munjiza, *The Combined Finite-Discrete Element Method*, John Wiley & Sons, London, UK, 2004.
- [30] A. Munjiza, T. Bangash, and N. W. M. John, “The combined finite-discrete element method for structural failure and collapse,” *Engineering Fracture Mechanics*, vol. 71, no. 4-6, pp. 469–483, 2004.
- [31] O. K. Mahabadi, A. Lisjak, A. Munjiza, G. Grasselli, and Y. Geo, “Y-geo: new combined finite-discrete element numerical code for g applications,” *International Journal of Geomechanics*, vol. 12, no. 6, pp. 676–688, 2012.
- [32] O. K. Mahabadi, G. Grasselli, A. Munjiza, and Y. Gui, “Y-GUI: a graphical user interface and pre-processor for the combined finite-discrete element code, Y2D, incorporating material heterogeneity,” *Computers & Geosciences*, vol. 36, no. 2, pp. 241–252, 2010.
- [33] B. S. A. Tatone and G. Grasselli, “A calibration procedure for two-dimensional laboratory-scale hybrid finite-discrete element simulations,” *International Journal of Rock Mechanics and Mining Sciences*, vol. 75, pp. 56–72, 2015.